CrossMark

EARTH-AFFECTING SOLAR TRANSIENTS

Deflection and Rotation of CMEs from Active Region 11158

Christina Kay[1] (iD) · Nat Gopalswamy[1] (iD) · Hong Xie[1,2] (iD) ·
Seiji Yashiro[1,2] (iD)

Abstract Between 13 and 16 February 2011, a series of coronal mass ejections (CMEs) erupted from multiple polarity inversion lines within active region 11158. For seven of these CMEs we employ the graduated cylindrical shell (GCS) flux rope model to determine the CME trajectory using both *Solar Terrestrial Relations Observatory* (STEREO) extreme ultraviolet (EUV) and coronagraph images. We then use the model called Forecasting a CME's Altered Trajectory (ForeCAT) for nonradial CME dynamics driven by magnetic forces to simulate the deflection and rotation of the seven CMEs. We find good agreement between ForeCAT results and reconstructed CME positions and orientations. The CME deflections range in magnitude between 10° and 30°. All CMEs are deflected to the north, but we find variations in the direction of the longitudinal deflection. The rotations range between 5° and 50° with both clockwise and counterclockwise rotations. Three of the CMEs begin with initial positions within 2° from one another. These three CMEs are all deflected primarily northward, with some minor eastward deflection, and rotate counterclockwise. Their final positions and orientations, however, differ by 20° and 30°, respectively. This variation in deflection and rotation results from differences in the CME expansion and radial propagation close to the Sun, as well as from the CME mass. Ultimately, only one of these seven CMEs yielded discernible *in situ* signatures near Earth, although the active region faced toward Earth throughout the eruptions. We suggest that the differences in the deflection and rotation of the CMEs can explain whether each CME impacted or missed Earth.

Keywords Sun: coronal mass ejections (CMEs) · Trajectory · Modeling

✉ C. Kay
christina.d.kay@nasa.gov

[1] Solar Physics Laboratory, NASA Goddard Space Flight Center, Greenbelt, MD, USA

[2] Department of Physics, The Catholic University of America, Washington, DC, USA

2 Springer

1. Introduction

Understanding the path that a coronal mass ejection (CME) takes as it propagates away from the Sun is essential for predicting any space weather effects the CME may induce at Earth or elsewhere in the heliosphere. While current efforts have focused on predicting when a CME will impact Earth (*e.g.* Mays *et al.*, 2015, and references within), one must first understand whether a CME will impact Earth, and even which part of the CME will yield the impact. This requires knowledge of any CME deflection – a deviation in latitude, longitude, or both, from a perfectly radial trajectory. Additionally, CME rotations, that is, changes in the orientation of the CME, can also have significant effects.

CME deflections have been observed since the earliest spaceborne coronagraph measurements (Hildner, 1977; MacQueen, Hundhausen, and Conover, 1986). Hildner (1977) noted a systematic motion of CMEs toward the solar equator in the *Skylab* observations. MacQueen, Hundhausen, and Conover (1986) still found evidence of deflections in the *Solar Maximum Mission* observations, but the systematic equatorward motion no longer occurred. With the launch of the twin *Solar Terrestrial Relations Observatory* (STEREO) spacecraft, CMEs could be observed from more than a single viewpoint. These additional perspectives, combined with stereoscopic reconstruction techniques, confirmed that deflections could occur in both latitude and longitude (*e.g.* Isavnin, Vourlidas, and Kilpua, 2013; Liewer *et al.*, 2015).

Deflections were initially correlated with the relative positions of coronal features such as the heliospheric current sheet (HCS) and coronal holes (CHs). The deflection motion was frequently described as toward the HCS (Cremades and Bothmer, 2004; Kilpua *et al.*, 2009) or away from CHs (Gopalswamy *et al.*, 2009). Typically, these two directions tend to be aligned because the HCS and CHs are intrinsically coupled by the solar magnetic field. On global scales, CHs tend to be the regions of highest magnetic field strength, outside of active regions, and the HCS tends to be the region of lowest magnetic field strength. The solar magnetic field reverses radial direction at HCS, which causes a decrease in the magnetic field strength near the HCS. The magnetic field in models often becomes zero near the HCS, but while observations show a decrease in the magnetic strength near the HCS, it is still nonzero due to the tangential field components (*e.g.* Gosling *et al.*, 2005). Magnetic forces may be the mechanism responsible for CME deflections because on global scales they will produce the same general trends as seen in observations (Filippov, Gopalswamy, and Lozhechkin, 2001; Gopalswamy *et al.*, 2009; Shen *et al.*, 2011; Gui *et al.*, 2011; Kay, Opher, and Evans, 2015). Related to the rolling motion of eruptive prominences (Panasenco *et al.*, 2011, 2013), in the low corona they may be caused by smaller scale magnetic gradients related to the structure of active regions (ARs) or to local magnetic null points (Kay, Opher, and Evans, 2015).

Deflection toward the HCS and the variation in its position over the solar cycle, could explain the difference in the observations of Hildner (1977) and MacQueen, Hundhausen, and Conover (1986), which respectively occurred in solar minimum and maximum. During solar minimum, the HCS is flat and near the equator and CHs are located near the poles, so that primarily equatorward deflections should occur. However, as the Sun approaches solar maximum, the HCS becomes inclined and the CHs extend to low latitudes, so that a wider range of deflections will occur.

Observations show evidence for CME rotation in the corona (*e.g.* Vourlidas *et al.*, 2011; Nieves-Chinchilla *et al.*, 2012; Thompson, Kliem, and Török, 2012). It is difficult to distinguish the effects of CME deflection, rotation, and expansion in the low corona (Savani *et al.*, 2010; Nieves-Chinchilla *et al.*, 2013), but CME rotation is also observed in simulations due to a variety of mechanisms (Török and Kliem, 2003; Fan and Gibson, 2004; Lynch *et al.*, 2009). Simulated rotations such as the ones described in the previous articles tend to occur
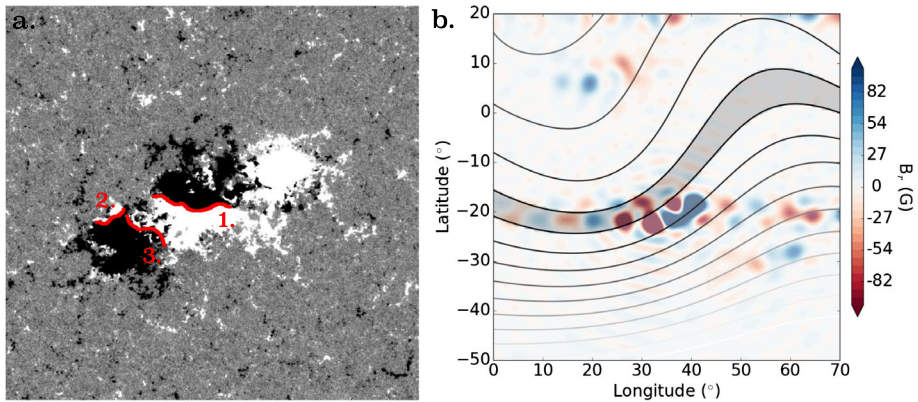
Figure 1 The left panel shows an image of AR 11158 from HMI from 14 February 2011 at 03:30 UT. The red lines indicate the three different PILs. The right panel shows the results of a potential field source surface (PFSS) magnetic field model with color regions of the surface magnetic field near AR 11158 (at 1 R_S) and line contours of the magnetic field farther out (2.5 R_S) projected onto the solar surface. The gray region indicates the location of the heliospheric current sheet, approximated by the location of the weakest magnetic field strength. Panel b shows a much larger field of view than panel a with the AR in the HMI magnetogram corresponding to the enhanced magnetic field in the center of the color regions of the surface PFSS magnetic field.

as a result of the kink instability, and the direction of the rotation is then directly related to the handedness of the flux rope magnetic field. Better understanding of the rotation of CMEs is needed to understand the expected orientation of CMEs upon impact at Earth.

In this article we study the deflections and rotations of seven CMEs that erupted from the same AR. In particular, we compare the similarities and differences in their trajectories and seek explanation for the differences between their evolutions. In Section 2 we describe the CME source, AR 11158, and our reconstruction of the CME positions from coronagraph observations. In Section 3 we describe a model called Forecasting a CME's Altered Trajectory (ForeCAT), to calculate for CME deflections and rotations based upon magnetic forces, which we use to simulate each of the seven CMEs, shown in Section 4. Finally, in Section 5 we discuss the implications of the different CME deflections and rotations.

2. Observations

AR 11158 was extremely active between 13 and 16 February 2011, and it remained facing toward Earth the entire time. During this time span, 21 flares occurred in AR 11158, ranging from C4.2 up to X2.1 according to the GOES X-ray classification. Six of the flares were M1.0 class or greater, and these larger flares occurred uniformly throughout this time span. The flares occurred at three different polarity inversion lines (PILs) within the AR. Figure 1a shows an image of AR 11158 from the *Helioseismic and Magnetic Imager* (HMI: Schou *et al.*, 2012) onboard the *Solar Dynamics Observatory* (SDO: Pesnell, Thompson, and Chamberlin, 2012) with the red lines indicating the locations of the PILs. Two of these PILs were relatively horizontal (labeled 1 and 2 in Figure 1) – a small one to the northeast of the AR and a larger one slightly northwest of its center. The third PIL was relatively vertical and located between and slightly south of the other two PILs. We identify the location of each flare using SDO/*Atmospheric Imaging Assembly* (AIA: Lemen *et al.*, 2012) 94 Å images. Flaring was evenly distributed between the three PILs, with multiple PILs being in-

volved in several of the flares. Flares from the third vertical PIL (labeled 3) tended to occur at later times.

Eleven of these flares had associated CMEs. Unlike the flares, there is significant asymmetry in the temporal and spatial distribution of the CMEs. Ten of the first 11 flares have associated CMEs, but only one of the last ten flares is accompanied by a CME. The CMEs all erupt from one of the two horizontal PILs; no CMEs occur at the vertical PIL. The earlier CMEs tend to come from the larger, more westward PIL (hereafter PIL 1) and the later CMEs from the smaller, more eastward PIL (hereafter PIL 2).

We determine the trajectory of these CMEs by simultaneously fitting the graduated cylindrical shell (GCS) model (Thernisien, Howard, and Vourlidas, 2006) to coronagraph views from STEREO A and B/COR1 (Thompson *et al.*, 2003) using SolarSoft IDL procedures. When possible, we also use STEREO EUV images. All images are first processed using the secchi_prep routine. A wireframe CME model is then fit to the dual coronagraph views. The CME height, latitude, longitude, tilt, angular width, and a shape are adjusted by hand until a visual match is obtained. We fit each CME at multiple times throughout its evolution, obtaining the deflection and rotation of the CME from the change in its position and orientation. Throughout this work we refer to these reconstructed positions as the "observations" (as opposed to our simulated values). We emphasize that these values are in fact free parameters of the GCS model, which is itself highly uncertain due to the complex nature of the line-of-sight integrated coronagraph images. However, this technique of constraining the GCS parameters using multiple simultaneous coronagraph observations is still the best available means of determining the position and orientation of a CME.

We cannot fit all the CMEs from AR 11158. Several of the CMEs are too faint to reliably fit them using the GCS model. One of the CMEs interacts with a preceding CME from another AR, which we do not include because simulating this collision is beyond the scope of this work. We reproduce the trajectory for seven CMEs, one on 13, 15, and 16 February 2011, respectively, and four on 14 February 2011. We refer to the CMEs by their day of eruption and use suffixes of A through D to differentiate between the four occurring on 14 February, assigned in chronological order. Note that additional CMEs occurred on 14 February in between our reconstructed CMEs, but we do not consider them in our labeling scheme. Table 1 lists the seven CMEs, the time of our first measured position, and the PIL from which they erupted. Figure 2 shows the GCS model as a green wireframe overplotted on the STEREO A image for three of the CMEs (CME 13, 14A, and 14C, which have the largest deflections and rotations). The left column shows the closest measured CME position (from STEREO/*Extreme Ultraviolet Imager* (EUVI)) and the right column shows the farthest position (from STEREO/COR1). The CME is often difficult to resolve in the EUV, but an estimate of its location can be determined from the flare brightening and the known AR PIL location. The reconstructed CME latitude, longitude, and tilt (measured clockwise with respect to the solar equator) *versus* distance for all the CMEs are shown in Figures 3 and 4.

We assume error bars of 5° for the reconstructed latitude and 10° for the reconstructed longitude and tilt, standard values for visual GCS fits (Thernisien, Vourlidas, and Howard, 2009). We see that some of the CMEs show significant latitudinal deflections and rotations beyond the magnitude of the error bars. Because of the large uncertainty, however, most of the reconstructed longitudinal motion is consistent with no deflection. In some cases (CMEs 14B, 14D, and 15) we see little change in either the reconstructed latitude or tilt, but the value differs significantly from the initial latitude and tilt expected from our knowledge of the AR, which implies that significant evolution must have occurred before our first reconstructed points.

Table 1 Initial (0) and final (f) positions and orientations of the considered CMEs from the results of the ForeCAT simulations. The longitudes are given as Carrington longitudes.

CME	Date and time	PIL [UT]	Lat_0 [°]	Lat_f [°]	Lon_0 [°]	Lon_f [°]	$Tilt_0$ [°]	$Tilt_f$ [°]
13	13 Feb. 2011 17:35	1	−20.4	−11.1	35.6	39.2	−34.0	−81.4
14A	14 Feb. 2011 4:45	1	−20.7	−7.1	37.0	36.0	−25.0	−76.5
14B	14 Feb. 2011 7:15	2	−19.4	5.0	30.8	36.3	0.0	−40.9
14C	14 Feb. 2011 12:55	2	−18.9	7.8	31.5	20.5	30.0	37.5
14D	14 Feb. 2011 19:45	2	−20.6	−11.7	31.5	31.3	40.0	69.6
15	15 Feb. 2011 1:50	1	−19.0	−12.2	33.5	35.7	5.0	−12.6
16	16 Feb. 2011 14:25	2	−18.9	4.4	31.5	22.3	30.0	37.5

Figure 2 GCS reconstructed positions for CMEs 13B (top), 14A (middle), and 14C (bottom). The time corresponding to the first and last measured positions are shown on the left and right in the panels, respectively. The left column shows STEREO A/EUVI images and the right shows STEREO A/COR1 images with EUVI images in the center. STEREO A was located 87° west of the Earth during the observations. The red wireframe shows the GCS reconstruction of the CME at each height.
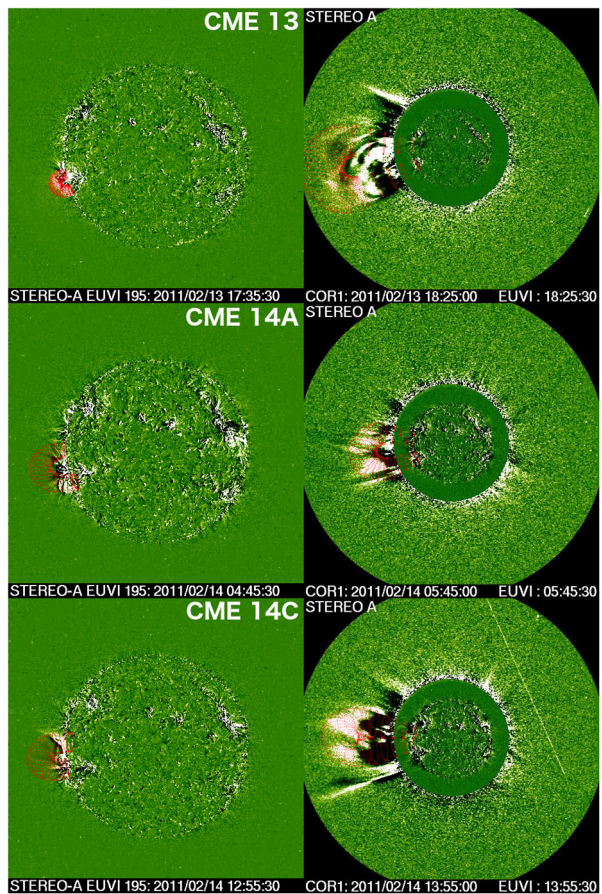
3. ForeCAT

Kay, Opher, and Evans (2013) first introduced the model called Forecasting a CME's Altered Trajectory (ForeCAT), which simulates CME deflections resulting from the magnetic forces of the background solar magnetic field. Kay, Opher, and Evans (2015) expanded upon ForeCAT, allowing for deflections in both latitude and longitude, and incorporated the effects of rotation that are due to differential deflection forces along the CME, which produce a torque about the CME nose. Note that this external torque can result in either rotation direction, whereas the kink-instability-driven rotation from the internal CME magnetic field, which is not currently included in ForeCAT, can only yield a single direction determined by the CME handedness. ForeCAT simulates the nonradial motion of a CME from the background magnetic tension and magnetic pressure gradients. To describe the background solar magnetic field, we use our own Python implementation of the PFSS model (Altschuler and Newkirk, 1969; Schatten, Wilcox, and Ness, 1969) computed from an HMI synoptic magnetogram and with the source surface set to the standard distance of 2.5 R_S. Figure 1b shows the PFSS model for Carrington rotation 2106 near AR 11158. The color regions show the magnetic field at the surface (1 R_S), which can be compared to the HMI observations in Figure 1a. The line contours show the magnetic field strength farther out (2.5 R_S), with

darker lines indicating weaker magnetic field strength. The gray shaded region indicates the minimum magnetic field strength, which corresponds to the location of the HCS. ForeCAT uses the direction of the magnetic field from the PFSS along with the shape and orientation of the CME to approximate the draping of the solar magnetic field about the CME. For a more thorough description of the ForeCAT model see Kay, Opher, and Evans (2015).

ForeCAT simulations require the initial position and orientation of the CME, which is constrained by the observed flare location, the CME shape, which is typically unconstrained, and the CME mass, angular width, and radial velocity as a function of time or radial distance. We use the coronal reconstructions to constrain the expansion and propagation. The CME mass, which we treat as constant in these cases, the CME shape, and the precise value of the initial latitude, longitude, and tilt are all free parameters. The best fit between the reconstructed deflection and rotation and the ForeCAT results allows us to constrain these previously unknown parameters.

ForeCAT currently requires an empirical model of a CME radial propagation and expansion. In this work we assume that all CMEs have a three-phase radial propagation, similar to that of Zhang and Dere (2006). A CME initially propagates with some minimum velocity, $v_{\min}$, until it reaches a radial distance R_1. Upon the CME nose reaching R_1, the CME begins accelerating at a linear rate until it reaches some final velocity, v_f, at R_2. We define the CME expansion in terms of half of the face-on angular width (hereafter angular width), which is the value returned from the SolarSoft GCS procedure. Since the GCS wireframe was fit to both STEREO spacecraft, as opposed to the view from the *Large Angle Spectrometric Coronagraph* (LACSO), we find a slight difference in the angular width as compared to the LASCO catalog,[1] which also quotes the full face-on angular width. We assume that the CMEs have an expansion that follows the form

$$\theta = \theta_0 + \theta_M\big(1 - \exp^{-(R-1)/R_\theta}\big),\tag{1}$$

where θ is the angular width of the CME, R is the radial distance of the CME nose from the Sun center, and θ_0, θ_M, and R_θ are free parameters. We also include a maximum angular width, θ_f, beyond which the angular width remains constant. We find that the deflection and rotation is not typically sensitive to this chosen θ_f since the magnetic forces have already become negligible by the distance the CME reaches θ_f.

It is often difficult to distinguish between CME deflection, rotation, and expansion in the low corona (*e.g.* Nieves-Chinchilla *et al.*, 2012), making precise observational determination of our model constraints implausible. Kay *et al.* (2016) show that ForeCAT can be used to better understand the early evolution of deflecting and rotating CMEs because we can identify and eliminate initial parameters that do not reproduce the observed behavior at farther distances. In this article we use the observations to constrain some parameters such as the final speed and angular width, but for the rest we must explore the parameter space and find those values that successfully reproduce the observed CME deflections and rotations. We explore the effects of differences in the expansion and propagation models.

4. Results

Using ForeCAT, we simulate each of the seven observed CMEs. Figure 1b shows that AR 11158 is located almost directly underneath, but slightly to the south of the HCS. We expect that deflection toward the HCS will move the CMEs slightly northward, but the deflection

---

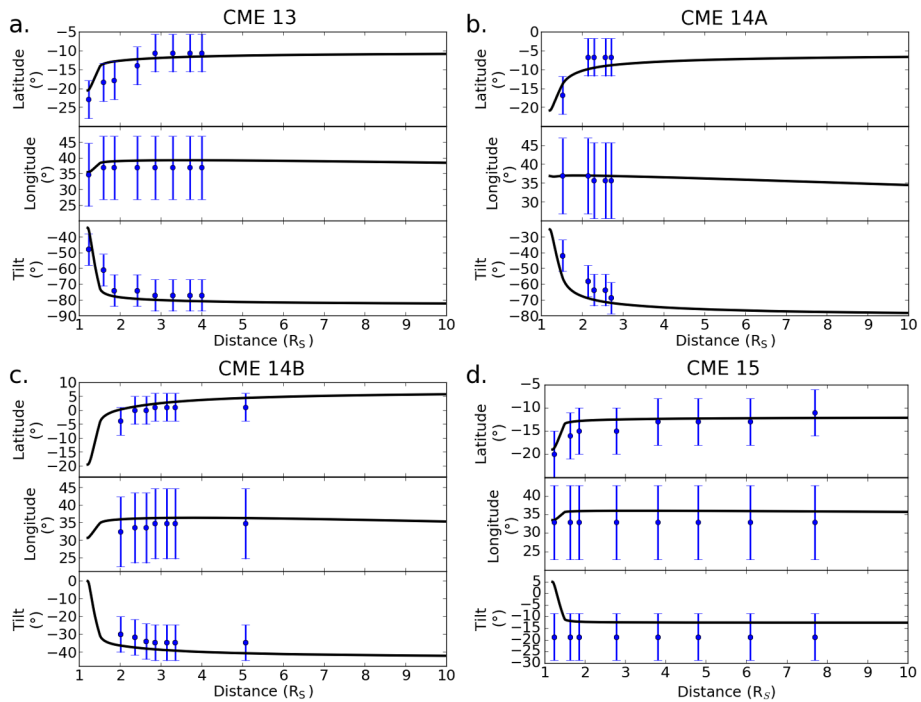[1] https://cdaw.gsfc.nasa.gov/CME_list/UNIVERSAL/2011_02/univ2011_02.html.

Figure 3 Comparison of the positions (latitude and longitude) and orientations of the reconstructed CMEs (blue circles) with the ForeCAT results (black lines) for four of the CMEs.

could continue east or westward along the current sheet, or be influenced by the small-scale gradients within the AR. Table 1 shows the initial and final CME positions from the ForeCAT simulations. The black lines in Figures 3 and 4 show the ForeCAT results. Figure 3 contains CMEs from both PIL 1 and 2, but the three CMEs included in Figure 4 are the three CMEs that erupted from PIL 2 and have initial positions within 2° from one another. For all seven CMEs we are able to reproduce the observed deflection and rotation within the limits of the reconstruction technique.

We first note that although they all originate from the same AR, the seven CMEs have very different behavior. All seven CMEs are deflected northward, but the magnitude of the latitudinal deflection varies between 8.9° and 26.7°. For all cases the latitudinal deflection exceeds the longitudinal deflection, which varies between 0.2° and 10°. Both eastward and westward deflections occur. We also see large differences in the CME rotation, with both clockwise and counterclockwise rotations occurring with magnitudes ranging between 5.7° and 51.5°.

For all CMEs we find a rapid deflection below about 2 R_S, after which the deflection either becomes negligible or proceeds at a much slower rate. This trend has been previously noted in Kay, Opher, and Evans (2013), Kay, dos Santos, and Opher (2015), and Kay and Opher (2015). When the deflection does continue beyond 2 R_S, this motion rarely exceeds an additional deflection of 5° in latitude or longitude. We see the same behavior for the CME rotation, with the most rapid rotation occurring below 2 R_S.

CMEs 13 and 14A both erupt from PIL 1, with similar initial latitudes, but with more than 1° difference in their initial latitude. Both CMEs are relatively weak and small, but CME 13 is slightly more massive (7×10^{14} g), faster (570 km s^{-1}), and has a larger angular width

**Figure 4** Same as Figure 3, but for the other three CMEs, which all have initial positions within 2° from one another.
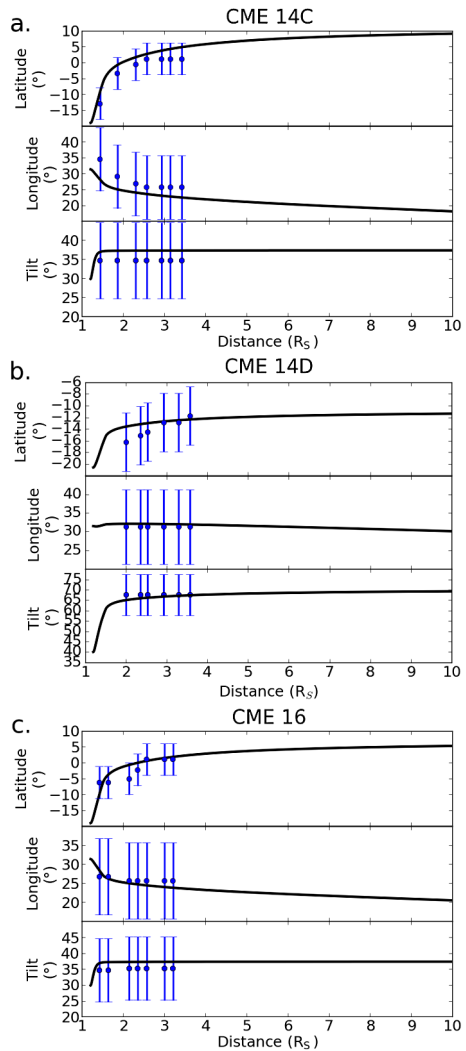
(22°) than CME 14A (4×10^{14} g, 300 km s^{-1}, 17°). Note that the masses are determined from the best-fit ForeCAT results and the speed and angular width are constrained by the observations. Figures 3a and b show relatively similar behavior for the two CMEs. Both are deflected northward and rotate clockwise to a nearly vertical orientation, but the magnitudes of the deflection and rotation are greater for CME 13. Neither CME exhibits a significant longitudinal deflection, but the direction of the motion differs for the two cases. CME 13 is continually deflected westward until the motion becomes negligible around 2 R_S, where CME 14A oscillates from east to west back to a final eastward motion. This shows the susceptibility of very low mass CMEs to differences in the local magnetic gradients in the low corona, but the net longitudinal motions remain small in this case.

Figure 3d shows CME 15, which is the most massive (10^{15} g), fastest (1600 km s^{-1}), and largest (37°) CME considered in this article. Compared to CMEs 13 and 14A, it erupts at a slightly higher latitude and more eastward longitude along PIL 1. CME 15 also begins with

Figure 5 Comparison of the
expansion (top) and radial
propagation (bottom) models
used for CMEs 14C (blue), 14D
(red), and 16 (purple). The
symbols indicate the angular
width reconstructed with the
GCS model or the average final
radial velocity determined from
the farthest three reconstructed
positions.
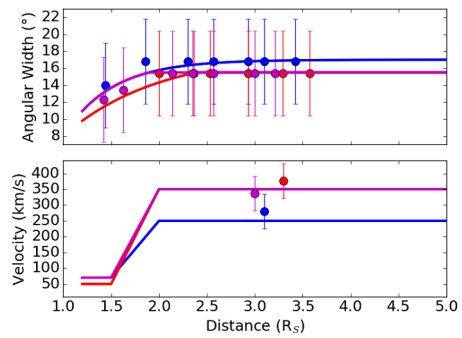
an orientation more parallel to the equator. Despite these differences, CME 15 shows the
same behavior as CME 13 and CME 14A (excluding the longitudinal oscillation), but the
magnitudes of the deflection and rotation are much smaller as a result of the increased CME
mass and speed.

CME 14B (Figure 3c), which erupts from PIL 2, is a relatively low-mass (5×10^{14} g),
slow (400 km s^{-1}), and small (17°) CME. It is deflected northward, similar to the PIL 1
CMEs, but with a significantly larger magnitude. The westward deflection is comparable
to that of CME 13. CME 14B rotates roughly 40° clockwise, comparable to but slightly
smaller than the clockwise rotations of CMEs 13 and 14A. CME 14B begins with a much
flatter orientation, so that it does not become nearly vertical like CMEs 13 and 14B.

CMEs 14C, 14D, and 16 (Figures 4a, b, and c, respectively) all erupt from PIL 2. The
three CMEs begin at the same longitude, but CME 14D has an initial latitude just below
2° south of the other two CMEs. The tilt of CME 14D is 10° larger (more inclined) than
the other two CMEs. All three CMEs are deflected northward and rotate counterclockwise.
CMEs 14C and 16 are deflected eastward, and CME 14D initially exhibits a small longi-
tudinal oscillation, similar to CME 14A, before it is deflected eastward. The deflection of
the CME 14D greatly exceeds that of either CME 14C or 16, which results from the slight
difference in its position and orientation.

Since these CMEs have such similar initial positions, we expect that the variations in
their behavior result from either difference in the CME mass or their expansion and radial
propagation. CMEs 14C and 16 are both very light CMEs with masses of only 3×10^{14} g,
whereas CME 14D is slightly more massive at 6×10^{14} g. CME 14C and 16 have the same
position, orientation, and mass, yet CME 14C has a noticeably larger deflection and rotation,
which must result from differences in their expansion and radial propagation. The deflection
of CME 14D is smaller than that of the other two cases, which can be explained by its higher
mass.

Figures 5a and b show the expansion and propagation models for CME 14C (blue), 14D
(red), and 16 (purple). These simple empirical functions relating the angular width or ra-
dial speed to the radial distance are technically inputs for the ForeCAT model. The CME
angular width and speed are more easily measurable beyond a few solar radii, but precise
values are difficult to determine in the low corona. We use the observed values from the final
reconstructed points (typically near 3 to 4 R_S) to constrain the empirical models as much as
possible. Typically, we can only constrain the low coronal evolution by determining which
values produce ForeCAT results that match the observations. Figure 5a shows the observed
angular width for each reconstructed distance with error bars of 5°. Figure 5b shows the
average final velocity determined from the last three reconstructed points with error bars of

55 km s^{-1}, which correspond to an uncertainty in the distance of 0.05 R_S and a time cadence of ten minutes. We do not include the velocity for each position as using a simple finite-difference derivative of the radial distance with respect to time yields values that vary by more than what is physically realistic.

CMEs 14C and 16 initially have the same angular width and radial velocity. At 1.5 R_S, both CMEs begin to accelerate from their initial radial speed values. CME 16 has a larger acceleration and reaches a higher final speed. Just before 2 R_S, CME 16 reaches its maximum angular width and stops overexpanding. CME 14C continues to slowly increase its angular width, reaching a final angular width slightly larger than that of CME 16. Both of these effects will cause an increase in the deflection of CME 14C relative to CME 16. The faster CME 16 spends less time in the region of strong magnetic forces and has a higher density since it has the same mass but a smaller angular size, so that it will gain less angular momentum than CME 14C. Additionally, if two CMEs have the same angular momentum, the CME with the slower radial velocity will have more time to be deflected before reaching a given radial distance, which will also increase the deflection of CME 14C relative to CME 16. Figure 4 shows that CMEs 14C and 16 behave similarly below 1.5 R_S, but their paths diverge when their propagation and expansion differ beyond this distance.

CME 14D initially has a smaller width than the other two CMEs and a lower initial radial velocity. While we would expect an increase in deflection as a result of the lower initial velocity, the higher CME mass and smaller angular width yield a greater CME density, allowing the CME to resist the magnetic deflection forces. Despite the smaller deflection, CME 14D undergoes a significant rotation. We expect that the differences in the expansion and propagation should uniformly affect the deflection and rotation, as for CMEs 14C and 16. Since the deflection of CME 14D decreases and the rotation increases relative to the other CMEs, we expect that this results primarily from the CME position and orientation. The net force on CME 14D may be more balanced, or the decrease in deflection may result from the increased CME density, but the increase in rotation corresponds to an increase in the torque on the CME. In Kay *et al.* (2016) we find that the rotation tends to be more sensitive to the small-scale local magnetic gradients, and therefore the initial location and orientation.

5. Discussion

To better compare the relative behavior of these CMEs, in Figure 6 we show the trajectories of all seven cases in three-dimensional space. Figure 6 shows one side and one front view, the sphere represents the Sun. The HMI magnetic field strength has been mapped onto the surface of the Sun. The online supplementary material includes a movie (AR11158.avi) showing the deflection and rotation of each CME (represented by a blue surface), comparing their trajectories from different angles. For each CME the blue surface represents the front of the CME and the black line traces the position of the CME nose. When we compare the trajectories, three of them are colored as in Figure 5. The overlap between the positions of CME 14 and CME 16 (blue and purple) close to the Sun can easily be seen in the front view.

At 10 R_S the latitudes of the CMEs vary between $-11.7°$ and $7.8°$, and the longitudes vary between $20.5°$ and $39.2°$. Figure 6 illustrates that even though all seven CMEs erupted from the same AR, they can take very different trajectories, and Figures 3 and 4 show that this is evident in both the observations and the simulations. The observations and simulations also show a wide range in CME rotation, with both clockwise and counterclockwise rotations occurring. All the CMEs from PIL 1 rotate clockwise, and all but one of the four

Figure 6 A side and front view comparing the trajectories of the seven CMEs out to 6 R_S. We use the same colors for the three CMEs as in Figure 5. The surface of the Sun is colored according to the radial magnetic field strength from HMI. A movie version is available in the online supplementary material.
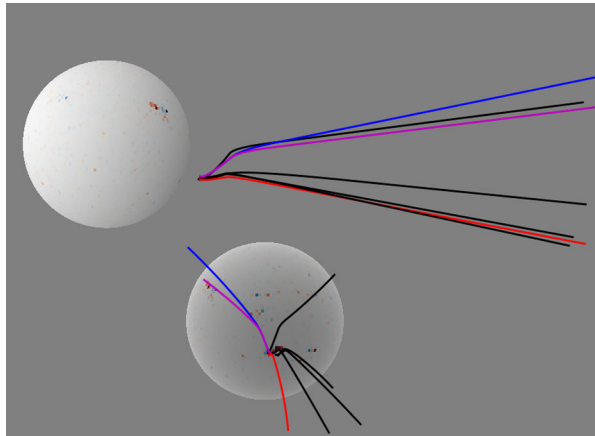
CMEs from PIL 2 rotate counterclockwise. Tziotziou, Georgoulis, and Liu (2013) show that during its evolution, AR 11158 builds up large amounts of right-handed helicity, suggesting that the erupting flux ropes would likely all be right handed. In this case, only a clockwise rotation should occur because of the internal CME torques. Two of the simulated counterclockwise rotations are on the order of 5° and the corresponding observations are consistent with no rotation, but CME 14D shows 30° of counterclockwise rotation in the observations, and the ForeCAT simulation shows that this motion can be reproduced by the external torques.

If space weather forecasters hope to predict CME impacts at Earth, it is essential to account for such varied deflections that can occur from a single AR. Additionally, HMI daily magnetograms show a significant evolution of AR 11158 during the eruptions, but we were able to reproduce the behavior of all seven CMEs using a single synoptic magnetogram. We suggest that for these deflections the large-scale gradients, which vary less on a day-to-day timescale, must have a stronger influence than the smaller, more rapidly varying magnetic gradients.

Another important aspect for predicting CME impacts is the location of the source region relative to the Earth. AR 11158 is relatively facing Earth from 13 to 16 February 2011, but due to the roughly 27-day rotation period of the Sun, the active region moves almost 28° in this time span. CME 13 erupts from a Stonyhurst longitude of −3.8° (measured with respect to the Earth longitude), whereas CME 16 erupts from a Stonyhurst longitude of 29.9°, although their Carrington longitudes differ by only 4.1°. We find that the final Stonyhurst longitudes of the CMEs vary between −8.4° and 20.7°.

Kay *et al.* (2017) suggest that two parameters, the normalized angular distance between the CME nose and the Earth, and the relative orientation of the CME tilt and the position angle of the Earth with respect to the CME nose, can be used to predict whether a CME will impact Earth. CME 15 is the only CME from this article that has a counterpart that appears in published lists of interplanetary coronal mass ejections (ICMEs), such as the Richardson and Cane (2010) list,[2] although AR 11158 is relatively facing Earth the entire time. CME 15 arrived at Earth on 18 February 2011, at 01:30 UT, significantly delayed from the predicted arrival time because of its passage through several smaller CMEs (Gopalswamy *et al.*, 2013). Using the criteria in Kay *et al.* (2017), we would only expect CMEs 13, 14A, and 15 to

---

[2]Updated list at http://www.srl.caltech.edu/ACE/ASC/DATA/level3/icmetable2.htm.

impact Earth. CMEs 13 and 14A, however, were very small and slow, so that the rapid CME 15 may have reached them and severely disrupted them or amassed them in its swept-up solar wind.

Olmedo *et al.* (2012) also study the CME on 15 February 2011, specifically the interaction between a coronal hole and an EUV wave associated with the CME. The wave propagating to the south is reflected off a coronal hole to the south. We suggest that the wave behavior may be explained by the motion of the CME edge, which results from a balance of the deflection, rotation, and expansion. Our simulated CME shows a change in the direction of its southern edge as it initially deflects northward faster than the bottom edge expands southward, then the motion reverses as the deflection slows and the expansion takes over. This is not the same motion as in Olmedo *et al.* (2012), but our CME is quite simplified and we only consider the net effect of the forces upon a rigid CME torus. In a more complex treatment, where the individual sections of the CME could evolve according to the local magnetic forces, the behavior of the CME edges could mirror the EUV wave.

6. Conclusion

AR 11158 was one of the most active ARs of Solar Cycle 24, producing 21 flares, including the first X-class flare of the cycle, and 11 CMEs over a span of four days. Here we use STEREO coronagraph images to determine the trajectory of seven of the CMEs. These trajectories, combined with our knowledge of the initial location of each CME, show that many of these CME underwent significant deflections and rotations. The reconstructed CME trajectory often shows little deflection or rotation beyond 2 R_S, so that we can only infer that deflection or rotation has occurred based on the difference from the initial CME location and orientation. We simulate all seven CMEs using ForeCAT, which confirms the expected deflection and rotation between the initial CME position and the closest reconstructed position. For all seven cases, the ForeCAT results match the reconstructed deflection and rotation within the uncertainty of the reconstruction technique.

The CMEs can be separated into eruptions from two different PILs. All CMEs show a northward deflection, with the magnitude ranging between 9° and 27°, which tends to scale with the CME mass. Most of the CMEs exhibit small longitudinal deflections (less than approximately 5°), but two of the CMEs (both from the more eastward PIL) show significant eastward deflections on the order of 10°. The CME rotations vary in magnitude between 5° and 50° and occur in clockwise and counterclockwise directions from both PILs.

Although they all originate from a single AR, we find very different behavior for the seven CMEs. The uniform northward motion corresponds to a deflection toward the HCS. We expect that the large latitudinal deflections result from this coherent force integrated over the CME, whereas the smaller longitudinal motion results from smaller-scale magnetic gradients that are related to the structure of the AR. For most of these CMEs, the varied longitudinal forces tend to balance out when averaged over the CME. For three CMEs with very similar initial positions and orientations, we find that the differences in their deflections and rotations can be explained by differences in their expansion, radial propagation, and mass. Finally, we suggest that the deflection and rotation can explain why only one of the seven CMEs had clear *in situ* signatures near Earth, although the AR faced Earth for all of the eruptions.

Disclosure of Potential Conflicts of Interest   The authors declare that they have no conflicts of interest.

References

Altschuler, M.D., Newkirk, G.: 1969, Magnetic fields and the structure of the solar corona. I: Methods of calculating coronal fields. *Solar Phys.* **9**, 131. DOI. ADS.

Cremades, H., Bothmer, V.: 2004, On the three-dimensional configuration of coronal mass ejections. *Astron. Astrophys.* **422**, 307. DOI. ADS.

Fan, Y., Gibson, S.E.: 2004, Numerical simulations of three-dimensional coronal magnetic fields resulting from the emergence of twisted magnetic flux tubes. *Astrophys. J.* **609**, 1123. DOI. ADS.

Filippov, B.P., Gopalswamy, N., Lozhechkin, A.V.: 2001, Non-radial motion of eruptive filaments. *Solar Phys.* **203**, 119. DOI. ADS.

Gopalswamy, N., Mäkelä, P., Xie, H., Akiyama, S., Yashiro, S.: 2009, CME interactions with coronal holes and their interplanetary consequences. *J. Geophys. Res.* **114**, A00A22. DOI. ADS.

Gopalswamy, N., Mäkelä, P., Xie, H., Yashiro, S.: 2013, Testing the empirical shock arrival model using quadrature observations. *Space Weather* **11**, 661. DOI. ADS.

Gosling, J.T., Skoug, R.M., McComas, D.J., Smith, C.W.: 2005, Magnetic disconnection from the Sun: Observations of a reconnection exhaust in the solar wind at the heliospheric current sheet. *Geophys. Res. Lett.* **32**, L05105. DOI. ADS.

Gui, B., Shen, C., Wang, Y., Ye, P., Liu, J., Wang, S., Zhao, X.: 2011, Quantitative analysis of CME deflections in the corona. *Solar Phys.* **271**, 111. DOI. ADS.

Hildner, E.: 1977, Mass ejections from the solar corona into interplanetary space. In: Shea, M.A., Smart, D.F., Wu, S.T. (eds.) *Study of Travelling Interplanetary Phenomena*, *Astrophys. Space Sci. Lib.* **71**, 3. ADS.

Isavnin, A., Vourlidas, A., Kilpua, E.K.J.: 2013, Three-dimensional evolution of erupted flux ropes from the Sun $(2 – 20\ R_S)$ to 1 AU. *Solar Phys.* **284**, 203. DOI. ADS.

Kay, C., Opher, M.: 2015, The heliocentric distance where the deflections and rotations of solar coronal mass ejections occur. *Astrophys. J. Lett.* **811**, L36. DOI. ADS.

Kay, C., dos Santos, L.F.G., Opher, M.: 2015, Constraining the masses and the non-radial drag coefficient of a solar coronal mass ejection. *Astrophys. J. Lett.* **801**, L21. DOI. ADS.

Kay, C., Opher, M., Evans, R.M.: 2013, Forecasting a coronal mass ejection's altered trajectory: ForeCAT. *Astrophys. J.* **775**, 5. DOI. ADS.

Kay, C., Opher, M., Evans, R.M.: 2015, Global trends of CME deflections based on CME and solar parameters. *Astrophys. J.* **805**, 168. DOI. ADS.

Kay, C., Gopalswamy, N., Reinard, A., Opher, M.: 2017, Predicting the Magnetic Field of Earth-impacting CMEs. *Astrophys. J.* **835**, 117. DOI. ADS.

Kay, C., Opher, M., Colaninno, R.C., Vourlidas, A.: 2016, Using ForeCAT deflections and rotations to constrain the early evolution of CMEs. *Astrophys. J.* **827**, 70. DOI. ADS.

Kilpua, E.K.J., Pomoell, J., Vourlidas, A., Vainio, R., Luhmann, J., Li, Y., Schroeder, P., Galvin, A.B., Simunac, K.: 2009, STEREO observations of interplanetary coronal mass ejections and prominence deflection during solar minimum period. *Ann. Geophys.* **27**, 4491. DOI. ADS.

Lemen, J.R., Title, A.M., Akin, D.J., Boerner, P.F., Chou, C., Drake, J.F., *et al.* 2012, The Atmospheric Imaging Assembly (AIA) on the Solar Dynamics Observatory (SDO). *Solar Phys.* **275**, 17. DOI. ADS.

Liewer, P., Panasenco, O., Vourlidas, A., Colaninno, R.: 2015, Observations and analysis of the non-radial propagation of coronal mass ejections near the Sun. *Solar Phys.* **290**, 3343. DOI. ADS.

Lynch, B.J., Antiochos, S.K., Li, Y., Luhmann, J.G., DeVore, C.R.: 2009, Rotation of coronal mass ejections during eruption. *Astrophys. J.* **697**, 1918. DOI. ADS.

MacQueen, R.M., Hundhausen, A.J., Conover, C.W.: 1986, The propagation of coronal mass ejection transients. *J. Geophys. Res.* **91**, 31. DOI. ADS.

Mays, M.L., Taktakishvili, A., Pulkkinen, A., MacNeice, P.J., Rastätter, L., Odstrcil, D., Jian, L.K., Richardson, I.G., LaSota, J.A., Zheng, Y., Kuznetsova, M.M.: 2015, Ensemble modeling of CMEs using the WSA–ENLIL + Cone model. *Solar Phys.* **290**, 1775. DOI. ADS.

Nieves-Chinchilla, T., Colaninno, R., Vourlidas, A., Szabo, A., Lepping, R.P., Boardsen, S.A., Anderson, B.J., Korth, H.: 2012, Remote and *in situ* observations of an unusual Earth-directed coronal mass ejection from multiple viewpoints. *J. Geophys. Res.* **117**, 6106. DOI. ADS.

Nieves-Chinchilla, T., Vourlidas, A., Stenborg, G., Savani, N.P., Koval, A., Szabo, A., Jian, L.K.: 2013, Inner heliospheric evolution of a "stealth" CME derived from multi-view imaging and multipoint *in situ* observations. I. Propagation to 1 AU. *Astrophys. J.* **779**, 55. DOI. ADS.

Olmedo, O., Vourlidas, A., Zhang, J., Cheng, X.: 2012, Secondary waves and/or the "reflection" from and "transmission" through a coronal hole of an extreme ultraviolet wave associated with the 2011 February 15 X2.2 flare observed with SDO/AIA and STEREO/EUVI. *Astrophys. J.* **756**, 143. DOI. ADS.

Panasenco, O., Martin, S., Joshi, A.D., Srivastava, N.: 2011, Rolling motion in erupting prominences observed by STEREO. *J. Atmos. Solar-Terr. Phys.* **73**, 1129. DOI. ADS.

Panasenco, O., Martin, S.F., Velli, M., Vourlidas, A.: 2013, Origins of rolling, twisting, and non-radial propagation of eruptive solar events. *Solar Phys.* **287**, 391. DOI. ADS.

Pesnell, W.D., Thompson, B.J., Chamberlin, P.C.: 2012, The Solar Dynamics Observatory (SDO). *Solar Phys.* **275**, 3. DOI. ADS.

Richardson, I.G., Cane, H.V.: 2010, Near-Earth interplanetary coronal mass ejections during Solar Cycle 23 (1996–2009): Catalog and summary of properties. *Solar Phys.* **264**, 189. DOI. ADS.

Savani, N.P., Owens, M.J., Rouillard, A.P., Forsyth, R.J., Davies, J.A.: 2010, Observational evidence of a coronal mass ejection distortion directly attributable to a structured solar wind. *Astrophys. J. Lett.* **714**, L128. DOI. ADS.

Schatten, K.H., Wilcox, J.M., Ness, N.F.: 1969, A model of interplanetary and coronal magnetic fields. *Solar Phys.* **6**, 442. DOI. ADS.

Schou, J., Scherrer, P.H., Bush, R.I., Wachter, R., Couvidat, S., Rabello-Soares, M.C., Bogart, R.S., Hoeksema, J.T., Liu, Y., Duvall, T.L., Akin, D.J., Allard, B.A., Miles, J.W., Rairden, R., Shine, R.A., Tarbell, T.D., Title, A.M., Wolfson, C.J., Elmore, D.F., Norton, A.A., Tomczyk, S.: 2012, Design and ground calibration of the Helioseismic and Magnetic Imager (HMI) instrument on the Solar Dynamics Observatory (SDO). *Solar Phys.* **275**, 229. DOI. ADS.

Shen, C., Wang, Y., Gui, B., Ye, P., Wang, S.: 2011, Kinematic evolution of a slow CME in corona viewed by STEREO-B on 8 October 2007. *Solar Phys.* **269**, 389. DOI. ADS.

Thernisien, A., Vourlidas, A., Howard, R.A.: 2009, Forward modeling of coronal mass ejections using STEREO/SECCHI data. *Solar Phys.* **256**, 111. DOI. ADS.

Thernisien, A.F.R., Howard, R.A., Vourlidas, A.: 2006, Modeling of flux rope coronal mass ejections. *Astrophys. J.* **652**, 763. DOI. ADS.

Thompson, W.T., Kliem, B., Török, T.: 2012, 3D reconstruction of a rotating erupting prominence. *Solar Phys.* **276**, 241. DOI. ADS.

Thompson, W.T., Davila, J.M., Fisher, R.R., Orwig, L.E., Mentzell, J.E., Hetherington, S.E., Derro, R.J., Federline, R.E., Clark, D.C., Chen, P.T.C., Tveekrem, J.L., Martino, A.J., Novello, J., Wesenberg, R.P., StCyr, O.C., Reginald, N.L., Howard, R.A., Mehalick, K.I., Hersh, M.J., Newman, M.D., Thomas, D.L., Card, G.L., Elmore, D.F.: 2003, COR1 inner coronagraph for STEREO-SECCHI. In: Keil, S.L., Avakyan, S.V. (eds.) *Innovative Telescopes and Instrumentation for Solar Astrophysics*, *Proc. SPIE* **4853**, 1. ADS.

Török, T., Kliem, B.: 2003, The evolution of twisting coronal magnetic flux tubes. *Astron. Astrophys.* **406**, 1043. DOI. ADS.

Tziotziou, K., Georgoulis, M.K., Liu, Y.: 2013, Interpreting eruptive behavior in NOAA AR 11158 via the region's magnetic energy and relative-helicity budgets. *Astrophys. J.* **772**, 115. DOI. ADS.

Vourlidas, A., Colaninno, R., Nieves-Chinchilla, T., Stenborg, G.: 2011, The first observation of a rapidly rotating coronal mass ejection in the middle corona. *Astrophys. J. Lett.* **733**, L23. DOI. ADS.

Zhang, J., Dere, K.P.: 2006, A statistical study of main and residual accelerations of coronal mass ejections. *Astrophys. J.* **649**, 1100. DOI. ADS.